CHALMERS
UNIVERSITY OF TECHNOLOGY

Study of defluidization of iron- and manganese-based oxygen carriers under highly reducing conditions in a lab-scale fluidized-bed batch reactor

Fuel Processing Technology 219 (2021) 106874

Contents lists available at ScienceDirect

Fuel Processing Technology

journal homepage: www.elsevier.com/locate/fuproc

Study of defluidization of iron- and manganese-based oxygen carriers under highly reducing conditions in a lab-scale fluidized-bed batch reactor

Victor Purnomo [a,b,*], Duygu Yilmaz [b], Henrik Leion [b], Tobias Mattisson [a]

[a] Division of Energy Technology, Department of Space, Earth, and Environment, Chalmers University of Technology, Göteborg 412 58, Sweden
[b] Division of Energy and Materials, Department of Chemistry and Chemical Engineering, Chalmers University of Technology, Göteborg 412 58, Sweden

ARTICLE INFO

Keywords:
Defluidization
Oxygen carrier
Highly reducing environment
Chemical looping

ABSTRACT

Oxygen carriers play an important role in chemical looping processes to transport oxygen for fuel conversion. In this study, the defluidization phenomena of oxygen carriers were examined under highly reducing conditions in a fluidized-bed batch reactor. This is highly relevant to chemical-looping gasification, where oxygen carriers could be reduced to a significant extent compared to that in chemical-looping combustion. Only a few studies have reported the physical phenomena in a fluidized bed system under highly reducing conditions. Three iron- and two manganese-based oxygen carriers were investigated at 900 °C at several degrees of reduction in this study. Some oxygen carriers that have been exposed to several hours of operation in a 300 W chemical-looping reactor unit were also included in this study to provide a comparison to the fresh-calcined materials. Defluidization of particle beds occurred with the iron-based oxygen carriers, except for LD slag, which has a low content of iron. The defluidization was caused by the formation of elemental iron on the oxygen carriers' surface at high degree of reduction. All defluidizations occurred at a mass-based conversion ($\Delta\omega$) between 3.2–5.0%. The manganese-based materials were found to be less prone to defluidization.

1. Introduction

In the last decades, carbon capture and storage (CCS) has emerged as one of the promising concepts to overcome climate change that leads to global warming and many other environmental issues. Carbon dioxide (CO_2), which is considered as the main greenhouse gases that contribute to global warming, has been increasing rapidly in the earth's atmosphere due to various recent urban human activities [1]. Therefore, it is essential to reduce or even halt further carbon dioxide emissions, for example through CCS. One of the prominent ways to establish CCS is with chemical-looping technologies, in which direct contact between air and fuel is avoided, thus making the product gases nearly free from nitrogen [2].

Fig. 1 illustrates a generic chemical looping process that comprises two interconnected fluidized bed reactors. Oxygen carriers circulating between reactors are used to avoid direct contact between air and fuel. The oxygen carriers are oxidized in the air reactor (AR) based on the reaction of

$$O_2 + 2Me_xO_{y-1} \leftrightarrow 2Me_xO_y \quad (1)$$

and then circulated to the fuel reactor (FR), where fuels come in contact with oxygen transported by the oxygen carriers. The reduced oxygen carriers are then recirculated to the AR for recovery, thus completing the loop. This way the process eliminates the need of an additional air separation unit (ASU) since nitrogen is not mixed with the other gaseous products.

Three of the main chemical-looping processes are chemical-looping combustion (CLC), chemical-looping gasification (CLG), and chemical-looping reforming (CLR). While CLC has been extensively studied for a couple of decades, CLG and CLR recently gained more attention [3]. Table 1 shows the main differences between CLC, CLG, and CLR.

In the conventional CLC, many studies have reported that the change in the degree of oxidation of the oxygen carrier is generally quite high, perhaps less than 1 wt% on a mass-basis [4]. To facilitate syngas production in CLG or CLR, the amount of oxygen reacting in the FR is limited through allowing only partial oxidation of the oxygen carriers in the AR [5]. The use of oxygen carrier in CLG makes the production of a high-grade syngas that is nearly free of nitrogen possible without using pure oxygen [6]. Therefore, oxygen carriers are generally reduced to a

* Corresponding author at: Division of Energy Technology, Department of Space, Earth, and Environment, Chalmers University of Technology, Göteborg 412 58, Sweden.
E-mail address: purnomo@chalmers.se (V. Purnomo).

https://doi.org/10.1016/j.fuproc.2021.106874
Received 27 December 2020; Received in revised form 30 March 2021; Accepted 25 April 2021

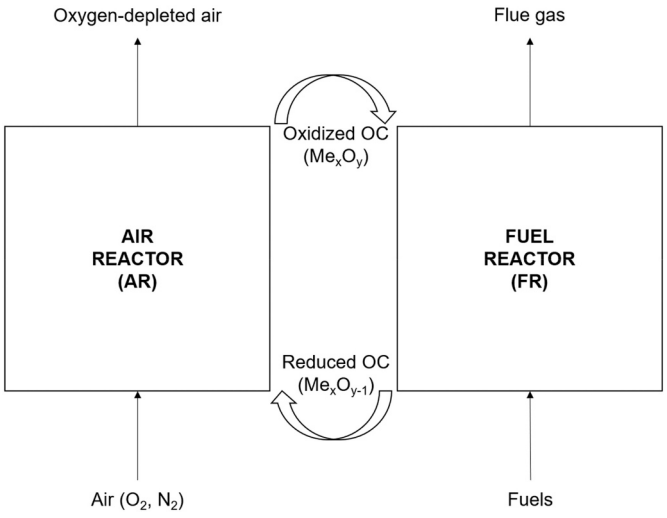

Fig. 1. Schematic diagrams of a chemical-looping process.

Table 1
Differences between CLC, CLG and CLR.

Subject	CLC	CLG	CLR
Main desired outcome and application	Heat and power generation for electricity, utilities, etc.	Syngas (CO + H_2) as a raw material for further processing	
Main constituents of the flue gas	CO_2, H_2O	CO, H_2, minor amounts of hydrocarbons	
Reaction taking place in the FR	C_nH_{2m} + *(2n + m)*Me_xO_y → nCO_2 + mH_2O + *(2n + m)* Me_xO_{y-1}	C_nH_{2m} + nMe_xO_y → nCO + mH_2 + nMe_xO_{y-1}	
Types of fuel	Gaseous/liquid/solid fuels	Solid fuels	Gaseous/ liquid fuels
OC oxidation in the AR	Close to full oxidation	Partial oxidation	
OC reduction in the FR	Low to moderate	Generally higher	

higher degree in CLG and CLR compared to in the CLC process. Higher degree of reduction may affect oxygen carriers' behavior, particularly in a fluidized bed system, which is the normal configuration for a chemical-looping system [7,8].

A good oxygen carrier is expected to have the following characteristics: high reactivity, high attrition resistance, low production cost and very low toxicity [9]. Recently, various iron- and manganese-based oxygen carriers have attracted interest to be used in CLC due to their favorable thermodynamic characteristics of fuel conversion [10] and also their abundant availability and environmentally friendly properties. Moreover, they are known as non-toxic and low-cost materials. However, there are limited studies about how they would behave under highly reducing conditions like in CLG or CLR, particularly with respect to their physical and chemical characteristics.

A handful of studies have been conducted on the mechanical and physical aspects that occur while oxygen carriers are being used in a fluidized bed system. One of these is the attrition of oxygen carrier particles. Werther and Reppenhagen [11] stated that interparticle collisions or collisions between the particles and a solid wall can lead to a mechanical stress that degrades the particles. Rydén et al. [12] investigated the attrition resistance of oxygen carrier and found that particles with higher crushing strength generally performed better than softer particles. Brown et al. [13] concluded that repeated cycling of reduction and oxidation resulted in a higher attrition rate of iron oxide particles. Furthermore, the agglomeration and defluidization of oxygen carrier are also issues of concern in a fluidized bed system. Some previous studies reported that these issues are closely related. Cho et al. [14] found that agglomeration of oxygen carrier particles may lead to defluidization of iron-based particles. Zevenhoven et al. [9] stated that oxygen carriers such as ilmenite may agglomerate under reducing conditions, especially upon interaction with ash and this can lead to defluidization.

This work reports on the experimental study of defluidization of low-cost Fe- and Mn-based oxygen carriers under various reducing conditions, which is relevant in selecting suitable oxygen carrier for processes like CLG or CLR. This sets this work apart from many of the studies above, where the main focus was on CLC, thus generally particles which had high degree of oxidation. Still, the results could also be applicable for normal CLC under certain conditions, for instance local variations in the bed. The work was conducted in a lab-scale batch fluidized-bed reactor by using syngas (50%CO and 50%H_2) as fuel. Pulse injection of CH_4 was also introduced after every syngas reduction to evaluate oxygen carrier reactivity with methane, an important component in solid fuel volatiles. Syngas was used here due to the reason of practicality as it reduces the oxygen carriers much faster, thereafter a pulse of methane was introduced to determine the reactivity in a more accurate way. The purpose of the work is to give a preliminary picture on oxygen carrier performance for CLG based on their physical and chemical behaviors under highly reducing condition. Particularly, the work aims to see how far an oxygen carrier can be reduced without tendencies for defluidization. When solid fuels are utilized, the bed will contain ashes which may also have implications for agglomeration and fluidization, but here the focus is on the oxygen carriers only. All oxygen carriers used in this work are either natural ores or industry wastes, thus the work shares interest with those who want to use low-cost materials as oxygen carriers in CLG or other related processes.

2. Materials and methods

2.1. Lab-scale batch fluidized-bed reactor setup

The reactor setup shown in Fig. 2 was designed to alternate the oxidation and reduction atmosphere around the oxygen carriers, in order to simulate what happens in a chemical-looping system.

The straight quartz glass reactor used in the study had an inner diameter of 22 mm and a height of 820 mm. Quartz can withstand a temperature up to 1100 °C. A bed material holder made of porous quartz was placed around 370 mm above the lower edge of the reactor. The reactor was put inside a furnace produced by ElectroHeat Sweden AB with gas-tight connections on its inlet and outlet. Upon heating up, a heating band was installed on the top of the reactor to maintain the high temperature in order to avoid gas condensation. Two thermocouples (Type K) were used to measure the real-time temperature inside the

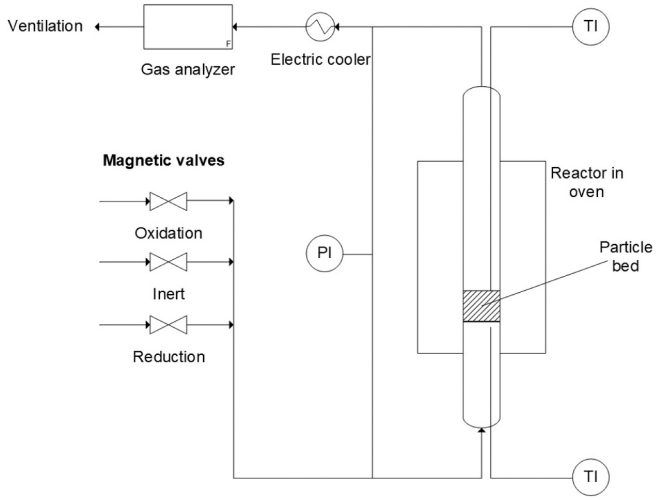

Fig. 2. A schematic system of the lab-scale fluidized-bed batch reactor.

particle bed and below the quartz plate. Three magnetic valves were installed to regulate gas flow to the reactor, i.e. oxidizing, inert, and reducing gases. M&C ECP1000 cooler was installed at the outlet to cool down the gas flow before entering the analyzer. Rosemount™ NGA 2000 gas analyzer measures the gas flow volumetric rates and the concentration of CO_2, CO, H_2, CH_4, and O_2. Leion et al. [15] have presented a more detailed presentation of the experimental system.

2.2. Fluidization monitoring system

A Honeywell pressure transducer with a frequency of 20 Hz was installed to measure the pressure difference between the reactor's top and bottom parts, meaning that the pressure drop is mainly associated with the quartz plate and the fluidizing particles. Despite having a relatively low frequency, the pressure transducer measurements were sufficient to monitor the bed fluidization of the system. Fig. 3 shows an example of how pressure difference monitor looked like when the particle bed of fresh-calcined ilmenite fluidized followed by a period when the same bed experienced defluidization.

Sudden pressure drops between each stage in the experiment, e.g. between inert 1 and reduction 1, were detected when changing the fluidization gas. This was due to the opening and closing of valves. The overall pressure drop was due to the presence of the quartz plate in the reactor, whose position is fixed and therefore creates some flow-dependent pressure difference, and does not necessarily indicate a defluidized bed. As long as the pressure fluctuation remains above the minimum standard deviation (SD) threshold the bed still fluidized. A separate observation in a cold flow experiment showed that the minimum SD of the pressure fluctuations of a fluidizing particle bed was 0.02 kPa. Thus, if the pressure fluctuations go below this threshold, the particle bed is assumed to have defluidized, which was confirmed in the cold-flow experiment. The SD ranges from 0.03–0.06 kPa when the bed fluidized in the batch reactor test, and hence the threshold was 0.03 kPa in this work.

2.3. Oxygen carriers

The oxygen carriers used in this work are presented in Table 2. The elemental analysis of these oxygen carriers has been given by several previous studies. The basis for the selection was that these oxygen carriers had been previously used for CLC with promising results. Furthermore, from sourcing different suppliers it was also established that these materials could be obtained at sufficient multi-ton scale, which is needed for future demonstration. With respect to the two manganese-based oxygen carriers, Sibelco and Elwaleed Grade B, it is clear that they have significant fractions of iron, especially the latter [16].

In this study, there are two states of oxygen carriers: fresh-calcined and used. The former refers to fresh oxygen carriers that were calcined in air at 950 °C for 24 h, except Sibelco which was already available in a calcined form. Calcination was done in order to eliminate the moisture content and ensure the full oxidation of oxygen carriers [22]. The latter are the fresh-calcined oxygen carriers that had been exposed to pilot-scale operation in a 300 W CLC unit for between 7 and 14 h using gaseous fuels [23,24]. The details of this unit was reported by Linderholm, et al. [25] All oxygen carriers were sieved to a size range of 125–180 μm prior to batch reactor tests. Observe that the Tierga ore was only available as fresh-calcined.

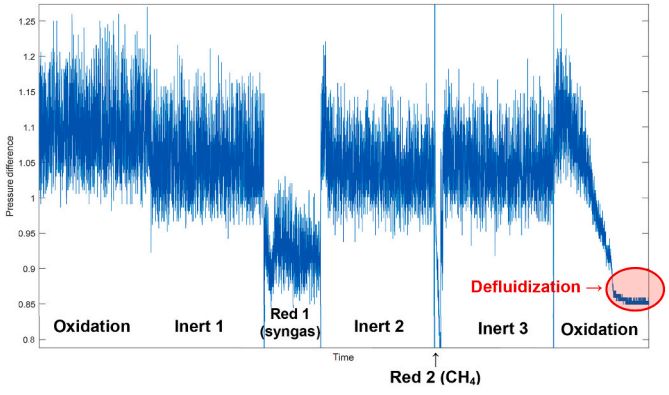

Fig. 3. Defluidization detected on the pressure difference monitor for an experiment with fresh-calcined ilmenite.

2.4. Experimental procedure

A sample of 15 g of each oxygen carrier were put inside the quartz reactor. Synthetic air (5% O_2 in N_2) was then introduced to the reactor which was heated inside the furnace until 850 °C. A pre-activation in syngas (50% CO and 50% H_2) was then performed for 3 cycles of 20 s. After that, the temperature was increased to 900 °C and the oxygen carrier was alternately oxidized with 5% O_2 in N_2 and reduced with syngas to different degrees. Between each step, nitrogen was introduced for 180 s to avoid gas mixing. The reduction period of syngas was extended gradually until either defluidization happened, i.e. when the SD of the pressure fluctuations decreased to below 0.02 kPa, alternatively when the outlet concentration of CO exceeded the concentration of CO_2. The latter indicates that the oxygen carrier ran out of available oxygen and was substantially reduced. Additionally, a short 10-s methane pulse was introduced after each reduction with syngas to evaluate oxygen carrier reactivity after each syngas reduction. This is because syngas is quite reactive to the oxygen carriers and nearly full gas conversion was always achieved with syngas, at least during the initial stages, thus it is difficult to establish the intrinsic reactivity of the solid material only using syngas conversion. Afterwards, the oxygen carrier was oxidized again, which marked the start of the next cycle, until the outlet concentration of O_2 was the same as that of the inlet, hence no more uptake of oxygen occurred. As a result of this, the time for oxidation increased as the oxygen carrier got further reduced.

By default, the experiments were set to stop when the samples were at a reduced state. Nonetheless, there were some experiments which were stopped during oxidation right after defluidization occurred. Since defluidization happened during the early stage of the oxidation, these samples were slightly oxidized. Despite not being the main focus of this work, the analysis of such samples can be used to evaluate the reproducibility of this study. When a material was later found to be defluidizing, a new fresh-calcined sample of the same material was retested in the batch reactor and reduced to a lower degree of reduction, also through several cycles. This was performed in order to provide a systematic comparison, particularly in terms of their constituent phases, with the highly reduced samples which defluidized. This was performed for several samples so that the collection of samples covers several degrees of reduction, ranging from the fresh one to the most reduced, defluidized sample.

Table 3 summarizes these steps with the corresponding volumetric flowrate, superficial velocity and ratio of fluidization velocity to the respective minimum fluidization velocity, which was calculated according to Wen and Yu correlation [26]. Furthermore, Table 4 shows the experimental matrix for every oxygen carrier. Generally, the initial reduction time was set to 20 s and this was then increased gradually by 20 s. There were some exceptions which were due to practicalities. For example, TOFC was initially reduced for 10 s to avoid reducing it too much further since the behavior of this material was still unknown at that time.

The concentration of outlet gases was measured throughout the experiment. Fig. 4 below shows the concentration profile from the gas outlet during a cycle of batch reactor test for ILFC.

The data was taken from a cycle when ILFC was reduced with syngas for 20 s at 900 °C. Under oxidation period, all the oxygen in the flow gas

Table 2
Oxygen carriers used in the experiment.

Oxygen carrier	Type	Elemental analysis of the fresh materials (wt%)						Sample codes	
		Mn	Fe	Si	Al	Ca	Ti	Fresh-calcined	Used
Ilmenite [17]	Fe-Ti ore	0.15	53.9	2.05	0.5	0.33	44.9	ILFC	ILAU
Tierga ore [18]	Fe ore	0.04	52.3	3.43	1.73	2.02	0.08	TOFC	None
LD slag [19]	Fe-Ca waste	3.6	24	10.2	1.3	49.5	1.1	LDFC	LDAU
Sibelco (calcined) [20]	Mn ore	46.1	5.18	3.74	3.39	2.02	0.23	SCFC	SCAU
Elwaleed Grade B [21]	Mn-Fe ore	32.4	21.7	4.67	1.22	1.71	0.08	EBFC	EBAU

Table 3
Steps in a cycle of batch reactor test.

Step	Time (s)	Injected gas	Q (mL/min)	ν (cm/s)	U/U_{mf}[a]
Heating/ Oxidation	Until outlet concentration of O2 returned to 5%	Synthetic air	1000	4.4	2.7–3.1
Inert 1	180	Pure nitrogen	900	3.9	2.5–3.3
Reduction 1	Various (see Table 4)	Syngas	600	2.6	2.2–3.0
Inert 2	180	Pure nitrogen	900	3.9	2.5–3.3
Reduction 2	10	Pure methane	450	1.9	1.7–2.3
Inert 3	180	Pure nitrogen	900	3.9	2.5–3.3

[a] Variations in the U/U_{mf} were due to different oxygen carrier densities.

Table 4
Experimental matrix for each oxygen carrier.

Oxygen carrier	Cycle and length of reduction with syngas, t_{syn} (s)
ILFC	3 × 20, 3 × 40, 5 × 60, 4 × 80, 1 × 90
ILAU1	3 × 20, 3 × 40, 3 × 60, 3 × 80, 1 × 90
ILAU2	3 × 40, 3 × 60, 3 × 80[a], 3 × 100[a], 2 x120[a]
TOFC	3 × 10, 4 × 20, 3 × 30, 5 × 40, 3 × 50, 4 × 60, 3 × 80, 3 × 100, 3 × 120, 3 × 140, 2 × 160
LDFC[b]	3 × 10, 4 × 20, 3 × 30, 3 × 40
LDAU[b]	3 × 10, 3 × 20, 3 × 30, 3 × 40
SCFC[b]	3 × 20, 6 × 40, 4 × 60
SCAU[b]	3 × 20, 6 × 40, 4 × 60
EBFC[b]	3 × 20, 3 × 40, 3 × 60, 3 × 80, 3 × 100, 3 × 120
EBAU[b]	3 × 20, 3 × 40, 3 × 60, 3 × 80, 3 × 100, 3 × 120

[a] The cycles where ILAU2 was oxidized at a lower temperature of 800 °C.
[b] The Mn-based ores were actually reduced further than indicated up to 360 s to the states where no observable conversion was seen.

was initially absorbed by the oxygen carrier before it returned to its original concentration, which was 5%, when the oxygen carrier was fully oxidized. In this cycle, nitrogen was introduced under the first inert period after 600 s of oxidation, making the oxygen concentration go down to zero. The length of oxidation can vary and depends on the temperature and how reduced the particles had been. When syngas was fed to the reactor under the first reduction period, a significant amount of CO_2 was formed due to the conversion of CO. All the gases were purged once again by nitrogen during the second inert period. A short methane pulse injection was then introduced for 10 s, in which a small amount of CO_2 and CO were formed as a result of the conversion of methane. It can be seen here that a significant amount of methane remained unconverted. The cycle ended with the third inert period where nitrogen was once again fed to the system before another cycle started.

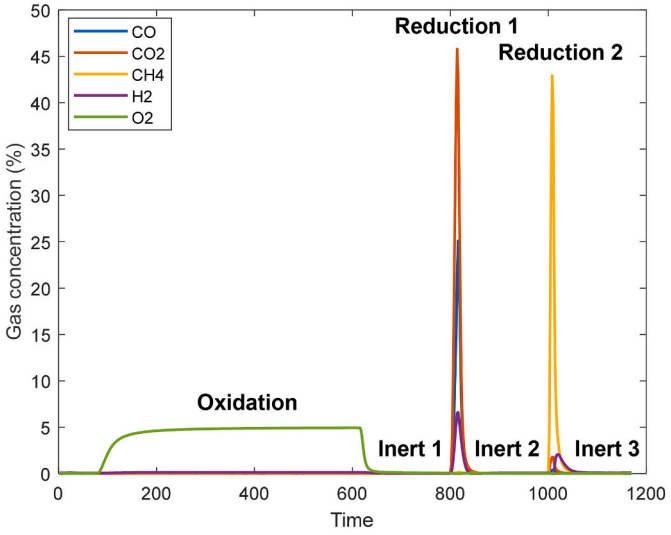

Fig. 4. Concentration profile from the gas outlet during a cycle of the batch reactor test for ILFC, Reduction 1 is the reduction with syngas and Reduction 2 is the methane injection.

2.5. Data evaluation

The mass conversion of the oxygen carrier under reduction with syngas and methane were calculated based on Eqs. (2) and (3), respectively.

$$\omega_{i,syngas} = \omega_{i-1} - \int_{t_0}^{t_1} \frac{\dot{n}\, M_O}{m_{ox}} (2x_{CO_2} + x_{CO} - x_{H_2})dt \tag{2}$$

$$\omega_{i,methane} = \omega_{i-1} - \int_{t_0}^{t_1} \frac{\dot{n}\, M_O}{m_{ox}} (4x_{CO_2} + 3x_{CO} - x_{H_2})dt \tag{3}$$

The final value of mass conversion was calculated as the sum of both mass conversion under reduction with syngas and methane as follows.

$$\omega_{i,final} = \omega_{i,syngas} + \omega_{i,methane} \tag{4}$$

The gas yield for reduction with syngas is defined as the fraction of outlet CO_2 divided by the sum of the fraction of the carbon-containing gases, i.e. CO and CO_2, in the outlet, as shown in Eq. (5).

$$\gamma_{syngas} = \frac{x_{CO_2}}{x_{CO_2} + x_{CO}} \tag{5}$$

Under reduction with methane, the CO_2-based gas yield and fraction of CO are defined by Eqs. (6) and (7), respectively. For the methane pulses, the average values of γ_{CO2} and γ_{CO} were calculated for the entire cycle in a certain t_{syn} from the integration of total molar flow of the corresponding gases.

$$\gamma_{CO_2,methane} = \frac{n_{CO_2}}{n_{CO_2} + n_{CO} + n_{CH_4}} \tag{6}$$

$$\gamma_{CO,methane} = \frac{n_{CO}}{n_{CO_2} + n_{CO} + n_{CH_4}} \quad (7)$$

2.6. Oxygen carrier characterization

The oxygen carriers, both before and after the experiments, which was in reduced form, were characterized with X-ray diffraction (XRD) Bruker D8 Advance to study the phase change on the oxygen carriers without any physical pretreatments. The defluidized oxygen carriers were observed under the light microscope Nikon SMZ800 to see how the particles appeared after experiments. These oxygen carriers were also embedded in epoxy and polished in order to display a cross section of the particles, and then analyzed by the elemental mapping feature of the SEM/EDX JSM-JEOL 7800F Prime.

3. Results and discussions

3.1. Syngas conversion

As the oxygen carriers were reduced, the mass-based conversions and gas yields changed over the reduction period, i.e. how long the particles were reduced in a cycle. Fig. 5 shows two different plots to demonstrate this. Fig. 5a shows the mass-based conversions plotted as a function of lengths of reduction for ILFC, while Fig. 5b shows the CO_2 gas yields as a function of mass-based conversions for (ILAU2). These plots were calculated based on Eqs. (2) and (5), respectively.

It is clear that mass-based conversion decreased as the length of reduction was increased. The lower the mass-based conversion, the higher the reduction degree. The decrease of mass-based conversion was almost linear to the increase of length of reduction. The CO_2-based gas yield also declined as the oxygen carriers were reduced further. It is worthy to note, however, that the initial values of gas yield were all about 90% and above, indicating that a high syngas conversion was always achieved. Some of the tested materials did show a lower initial gas yield at the beginning of the experiment, but the gas yield progressively increased as the length of reduction was gradually increased and until it eventually became stable. This indicated that such materials had not been fully activated despite the pre-activation steps. The subsequent redox cycles did activate the material, therefore the gas yield progressively increased as more pores and cracks formed on the particle surface before it reached a stable redox activity [27].

To provide a comparison with the other oxygen carriers, Fig. 6 shows the CO_2 gas yield plotted as a function of mass-based conversion in the last cycle in the batch reactor tests as indicated in Table 4.

All the plots show that a high CO conversion of more than 90% was achieved for both fresh-calcined and used iron-based oxygen carriers. The conversion of syngas with all materials decreased as the oxygen carriers were reduced further. All iron-based oxygen carriers had been reduced quite far before defluidization occurred, yet the syngas conversions remained above 55%. LD slag, a steel production waste, was an exception since its iron content was significantly lower.

The manganese-based materials also showed a high degree of syngas conversion at high degrees of mass-based conversion. Even though Sibelco had a lower degree of syngas conversion compared to Elwaleed B, its gas yield still reached around 80% at its lowest. The used Sibelco seemed to exhibit a higher and more sustaining syngas conversion trend compared to the fresh-calcined one. None of these particles defluidized despite being exposed to a very reducing environment, which is indicated by a low gas yield at the end of the reducing period. To demonstrate this, the fresh-calcined Sibelco (SCFC) was further reduced for 360 s as shown in Fig. 7. This is far beyond the oxygen carrier reduction degree at where the CO concentration was equal to the CO_2 concentration in the outlet, which was at $\Delta\omega = 1.7\%$.

It can be seen that when SCFC had been reduced to 4.3%, the syngas conversion dropped substantially to only 5%, yet even then the particles still did fluidize. This indicates that the manganese-based particles were less prone to defluidization even though they also contained some iron, as indicated in Table 1.

3.2. Defluidization of oxygen carriers

Defluidization happened on some oxygen carriers when reduced to a significant extent. The defluidizing oxygen carriers were ILFC, ILAU1, ILAU2, and TOFC, all iron-based natural ores. All defluidization, except ILAU2, occurred during the oxidation period. The oxygen carriers that eventually did not defluidize were reduced to various degrees until the CO concentration at least achieved the same level as the CO_2 concentration in the outlet, i.e. when there was no more significant conversion from CO to CO_2. It should be mentioned that LD slag and the manganese-based oxygen carriers were reduced even further, still no defluidization was observed. Table 5 shows a complete list of these mentioned parameters for both defluidized and non-defluidized materials.

Some experiments were repeated with the same iron-based materials that defluidized, i.e. ilmenite and Tierga ore, but using a lower oxidation temperature. The motivation for these experiments was that all defluidization occurred during the highly exothermic oxidation, and it was hypothesized that the observed defluidization could be related to melting at the surface. The oxidation temperature was set to 800 °C for

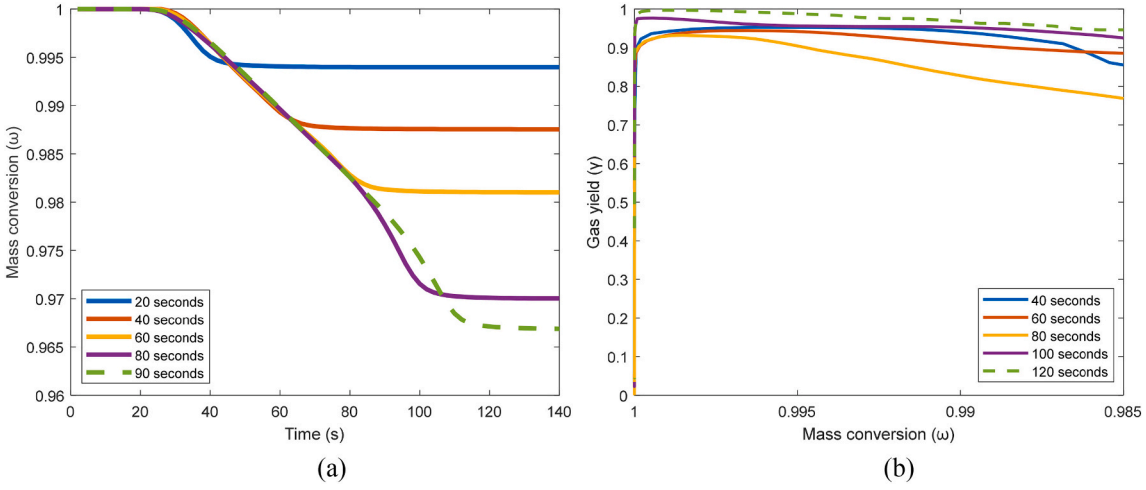

Fig. 5. The plots of (a) mass-based conversion as a function of length reduction for ILFC and (b) CO_2 gas yield as a function of mass-based conversion for ILAU2, both under syngas reduction. The dashed lines indicate the cycles that were followed by defluidization.

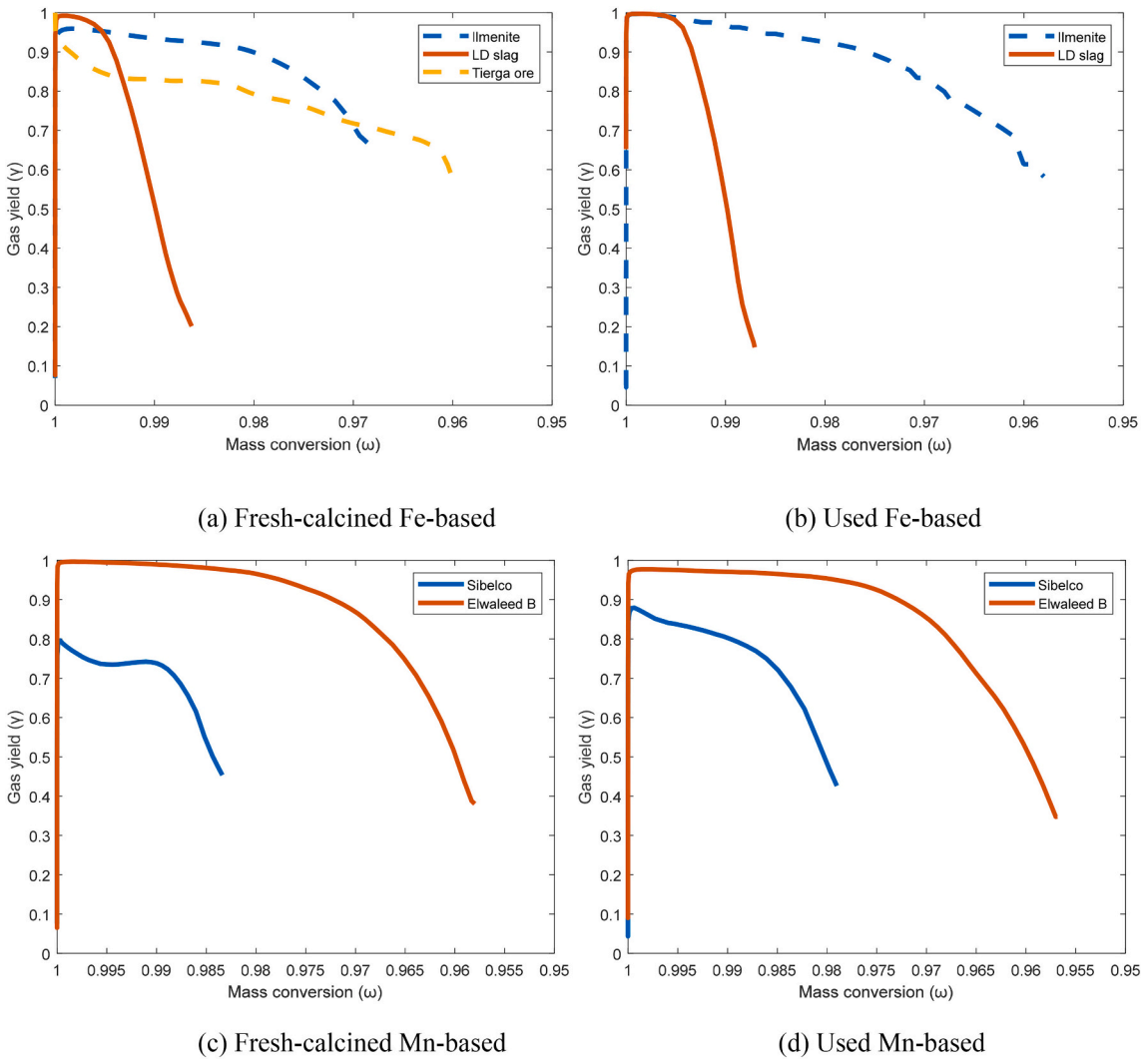

Fig. 6. CO_2 gas yield as a function of mass-based conversion under syngas reduction for every oxygen carrier at the last cycles in the batch reactor test. The dashed lines indicated the materials that eventually defluidized.

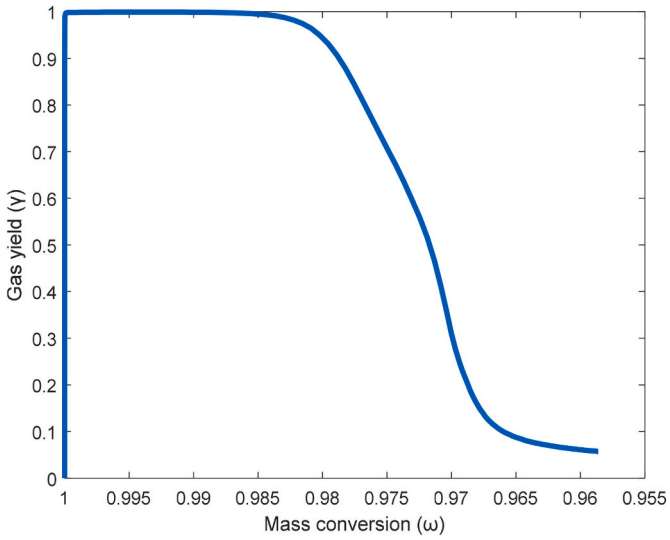

Fig. 7. CO_2 gas yield as a function of mass-based conversion under syngas reduction for SCFC reduced for 360 s.

the reduction period of 80 s and beyond. The results are provided in Table 6.

It is clear that the oxidation temperature affected the defluidization. The higher oxidation temperature, the higher the tendency for defluidization. The oxidation is always exothermic, which involves a substantial heat release. The released heat increases the particle temperature and could in some way affect the particles structure, especially if a temperature in any sites on the particle surface rise substantially to the melting point of the corresponding metals [28]. A more detailed explanation about melting points will be discussed later on. Furthermore, the sintering of iron powder is enhanced at high temperature and thus offers a favorable condition for defluidization. As will be discussed below, it is believed that metallic iron may play an important role in the agglomeration seen here. Once the temperature reaches the softening point of iron, the rate of sintering accelerates significantly and surface diffusion becomes important [29]. These possibilities for melting and stronger adhesion forces due to the sintering explain why defluidization on the particles oxidized at a higher temperature took place earlier than those that were oxidized at a lower temperature. For ILAU, however, the defluidization of the particle oxidized at 800 °C took place during reduction instead of oxidation, albeit a high degree of reduction. The used ilmenite, which can be assumed as a reduced ilmenite, tended to have more iron concentrated on the particle surface [30]. This can in some way increase the chance for defluidization to take place even

Table 5
Defluidization parameters of the oxygen carriers.

Oxygen carrier		Was defluidization observed?	Defluidized samples: State when defluidization was observed			Non-defluidized samples			
						State when the outlet concentration of CO equals to that of CO_2		State when the oxygen carrier was reduced the most	
			t_{red} (s)	Stage[a]	Δω (%)	t_{red} (s)	Δω (%)	t_{red} (s)	Δω (%)
Fe-based	ILFC	Yes	90	O	3.2	–	–	–	–
	ILAU1	Yes	90	O	3.7	–	–	–	–
	ILAU2	Yes	120	R	3.9	–	–	–	–
	TOFC	Yes	160	O	4.0	–	–	–	–
	LDFC	No	–	–	–	40	0.9	60	1.4
	LDAU	No	–	–	–	40	1.1	50	1.3
Mn-based	SCFC	No	–	–	–	60	1.7	360	4.3
	SCAU	No	–	–	–	60	2.1	80	2.6
	EBFC	No	–	–	–	120	4.2	160	4.4
	EBAU	No	–	–	–	120	4.3	120	4.3

[a] O = Oxidation, R = Reduction.

Table 6
Defluidization occurrences at different oxidation temperatures.

Oxygen carrier	State when defluidization was observed			
	Oxidized at 900 °C		Oxidized at 800 °C	
	State	Δω (%)	State	Δω (%)
ILFC	Oxidation	3.2	Oxidation	3.7
ILAU	Oxidation	3.7	Reduction	3.9
TOFC	Oxidation	4.0	Oxidation	5.0

during the reduction period.

3.3. Phase analysis of oxygen carriers

The phases of the iron-based oxygen carriers which at some points defluidized were analyzed by XRD at different stages of the reduction, which was done in order to establish a clear mechanism of their phase transformations. In addition to the samples that were reduced according to the experimental matrix in Table 4, some amount of the original materials, i.e. the materials before experiment, were reduced to lower reduction degrees through several cycles with different length of reduction. It should be noted that all the non-fresh samples were at reduced conditions when they were analyzed with XRD. Their main phases are summarized in Table 7. Here the index of each phase refers to the corresponding peak in the diffractogram, which can be seen in Fig. S.1 in the supplementary materials.

From the phase analysis by XRD, hematite (Fe_2O_3) was the main phase detected in ILFC and TOFC before experiment, which were fully oxidized. Apart from that, pseudrobrookite (Fe_2TiO_5) was also detected in the calcined ILFC. The oxidation of ilmenite taking place during the calcination performed at 950 °C can lead to the formation of Fe_2O_3.2-TiO_2 that eventually decomposed to pseudobrookite and rutile (TiO_2) [31]. Despite containing hematite, ILAU2 before the batch reactor test did not contain any pseudobrookite, which indicates that this material was not fully oxidized through calcination after the experiment in the continuous unit. Further, this material also contained the phase of magnetite (Fe_3O_4), which is one of the reduced phases of hematite. The phases of wüstite was detected in the reduced iron-based materials, particularly the ones that were reduced to 2.5% or further. It is worthy to note that most of the detected wüstite was non-stoichiometric. This is parallel with a study by Pineau, et al. [32] reporting that the reduction of magnetite at temperatures higher than 570 °C leads to the formation of non-stoichiometric wüstite.

Interestingly, the phase of elemental iron was only detected in the most reduced iron-based oxygen carriers, i.e. right before defluidization

Table 7
Main phases detected in the iron-based oxygen carriers.

Sample	Degree of reduction (%)	$Fe_2O_3^A$ (hematite)	$Fe_2TiO_5^B$ (pseudo-brookite)	$Fe_3O_4^C$ (magnetite)	$FeTiO_3^D$ (pure ilmenite)	FeO^E (wüstite)	Fe^F (elemental iron)	Iron titanium oxide phases
ILFC	Calcined	✓	✓	–	–	–	–	–
	1.1	–	✓	–	–	–	–	$Ti_xFe_{2-x}O_3$
	2.2	✓	–	✓	–	–	–	$Ti_xFe_{2-x}O_3$
	3.2 (defluidized)	–	–	✓	✓	✓ ($Fe_{1-x}O$)	✓	–
ILAU2	After-used	✓	–	✓	–	–	–	$Fe_3Ti_3O_{10}$, $Ti_xFe_{2-x}O_3$
	1.4	–	✓	✓ ($Fe_{3-x}O_4$)	–	–	–	$Ti_xFe_{2-x}O_3$
	2.5	–	✓ ($Ti_xFe_{2-x}O_5$)	✓ ($Fe_{3-x}O_4$)	–	✓ ($Fe_{1-x}O$, $Fe_{11}O_{12}$)	–	$Ti_xFe_{2-x}O_3$, $Ti_xFe_{3-x}O_4$
	3.9 (defluidized)	–	–	–	–	✓ ($Fe_{1-x}O$)	✓	$Fe_{3-x}Ti_xO_4$, $Ti_xFe_{2-x}O_3$
TOFC	Calcined	✓	–	–	–	–	–	–
	1.0	✓	–	✓ ($Fe_{3-x}O_4$)	–	–	–	–
	2.9	–	–	✓ ($Fe_{3-x}O_4$)	–	✓ ($Fe_{1-x}O$)	–	–
	4.0 (defluidized)	–	–	✓ ($Fe_{3-x}O_4$)	–	✓ (FeO, $Fe_{1-x}O$)	✓	–

✓: the phase was identified, –: the phase was not identified

occurred. Based on the Ellingham diagram for iron-oxygen system [33], it is possible to reduce wüstite (FeO) to elemental iron (Fe) at 900 °C when p_{CO}/p_{CO2} is higher than 1.2. Since the p_{CO}/p_{CO2} ratio was always lower than one for these defluidized materials, this indicated that the formation of elemental iron probably did not take place during reduction with syngas, but rather with methane instead. This was possible since the oxygen carrier has already been very reduced at this stage.

The oxidation of elemental iron generates much more heat compared to that released from the oxidation of the other iron oxides. To provide a comparison, Eqs. (8), (9) and (10) show the amount of heat released per mole of oxygen from several oxidation reactions calculated from the standard heat of formation of each compound [34].

$$\frac{4}{3}Fe_{(s)} + O_{2(g)} \rightarrow \frac{2}{3}Fe_2O_{3(s)} \Delta H^o = -553.7\ kJ\ mol\ O_2{}^{-1} = -415.12\ kJ\ mol\ Fe^{-1} \quad (8)$$

$$4Fe_3O_{4(s)} + O_{2(g)} \rightarrow 6Fe_2O_{3(s)} \Delta H^o = -516.4\ kJ\ mol\ O_2{}^{-1} \quad (9)$$

$$4FeO_{(s)} + O_{2(g)} \rightarrow 2Fe_2O_{3(s)} \Delta H^o = -579.6\ kJ\ mol\ O_2{}^{-1} \quad (10)$$

Since the oxidation of elemental iron was so exothermic, the temperature of the particle bed increased beyond the set reaction temperature, which was 900 °C. In the experiments, the measured increase in the temperature during oxidation was about 15 °C, but it should be pointed out that the local temperature on the particle surface could be substantially higher due to the oxidation on the surface. It is useful to compare these temperatures with the melting points of several phases of iron provided in Table 8.

It can be seen that these melting points are still higher than the highest recorded temperature of the particle bed. Nevertheless, the agglomeration of particles that led to defluidization could be caused by the sintering of particles, which can happen at a lower temperature. The sintering temperature of pure metal solid solutions ranges from 0.67 to 0.75 T_m, but that of mixed metal powders could be even lower [36]. Metal oxides, such as iron oxides, were also found to have lower sintering temperatures [37]. A study by Moulijn et al. [38] stated that sintering is highly temperature dependent and the mobility of aggregates can occur at substantially high temperatures. This means that even at a temperature lower than the melting points, the sintering of particles could take place, which leads to the formation of sinter necks and agglomerates, that thereby can cause the defluidization of the particle bed during oxidation.

Based on these facts, it could be estimated that the sintering temperature, assuming the ratio is 0.67, of the phase $FeTiO_3$ and FeO, is around 895 °C and 833 °C, respectively. These sintering temperatures are lower than the set reaction temperature of 900 °C. Considering that the phase of wüstite ($Fe_{1-x}O$) formed at rather high degrees of reduction, the sintering of wüstite can in some way promote the formation of particle agglomerates which eventually caused defluidization during oxidation, something which has also been reported by Cho et al. [14] However, as mentioned earlier, the local temperature on the particle surface could be significantly higher than the measured bed temperature, therefore it was possible that the sintering temperature of the other phases had been surpassed as well. Thus, it is not unlikely that the sintering of the other phases could have also caused the defluidization, yet the fact that metallic iron was detected in all defluidized samples suggests that this is an important phase.

Table 8
The melting points of several iron-based phases.

Phases	Melting point, T_m (°C) [35]
Fe_2O_3	1565
Fe_3O_4	1597
$FeTiO_3$	1470
FeO	1377
Fe	1538

Based on the reduction mechanism of wüstite to elemental iron reported by Liu et al. [39], it is clearly suggested that the elemental iron nucleates and grows on the surface of wüstite. It is possible that these separate nucleated elemental iron grains may have caused sticking problem in the fluidized bed, either between particles or between particles and the reactor walls [40]. This may have led to agglomeration of particles that eventually defluidized. This indicates that the formation of elemental iron on the surface of wüstite could be one of the factors that cause the defluidization.

In general, the formation of the phases of wüstite and elemental iron may not occur in the real CLG situation due to the high steam content in the reactor that prevent further reduction. However, it is important to note that it is not possible to ensure the uniformity of every part in the particle bed. This leads to a potential that the particle bed can be locally reduced much further than the rest of the bed in a certain operating mode and still can cause agglomeration and defluidization, at least partially. There are obviously many other factors that may cause such phenomena, yet a higher reducing condition is one of the most relevant situations in a real CLG process.

The phase analyses of the Mn-based oxygen carriers, i.e. fresh-calcined Sibelco and Elwaleed B both before and after the batch reactor tests, are shown in Fig. S.2 and summarized in Table 9. The mass-based conversions in the following table represent the final reduction degree to which materials had been reduced, thus they are not the same as those shown in Table 5.

The most reduced formed detected in the manganese-based materials was manganosite (MnO). This is expected since further reduction to elemental Mn is not possible in this case due to the thermodynamic limitations. Although the fresh-calcined manganese-based oxygen carriers contained some forms of iron, neither wüstite nor elemental iron was formed in their reduced forms. This is interesting considering EBFC contained quite significant percentage of iron and SCFC contained hematite (Fe_2O_3), the most oxidized phase of iron. The fact that iron in EBFC was contained in iron-manganese oxides may explain why the phases of wüstite and elemental iron did not form [41]. Further, hematite in SCFC did not reduce to either wüstite or elemental iron even though SCFC was reduced to a significant extent. This is indicated by the presence of a phase of iron-manganese alloy in its reduced form. A study by Zhang et al. [42] suggested that the reactions between FeO, SiO_2, and MnO can enhance the formation of a hard reductive (either Fe_2SiO_4 or Mn_2SiO_4), which can prevent the reduction of FeO to metallic iron. Even though none of the mentioned hard-reductive phases was detected by XRD in the reduced samples, the manganese-based oxygen carriers also contained SiO_2 and the phase of MnO was detected in the significantly reduced samples, thus it was not impossible for a similar kind of formation to take place. This could suggest that the presence of iron-manganese oxides in this material has in some way prevented the formation of metallic iron and therefore avoiding defluidization.

3.4. Imaging of oxygen carriers

The defluidizing oxygen carrier particles were observed under a light microscope. There were some agglomerates were seen and shown in Fig. 8.

Most of the particles that formed agglomerates in ILFC are grey. The particles that formed agglomerates in ILAU2 are mostly black, but some grey particles did form agglomerates as well. The largest agglomerate in TOFC observed under light microscope comprises both black and grey particles, but the edges between particles look rather grey. Apart from that, all particles that did not form agglomerate were all black. Here the appearance of grey and black colors can be assumed to represent the elemental iron [43] and wüstite [44], respectively. This is supported by the general knowledge that under no circumstances can metallic iron have a black color. Grey particles, which are assumed to have metallic iron on the surface, was to a much larger extent found in agglomerated

Table 9
Main phases detected in Sibelco and Elwaleed B samples.

Sample	Degree of reduction (%)	$Fe_2O_3^G$ (hematite)	$Mn_2O_3^H$	$Mn_3O_4^K$ (hausmannite)	MnO^L (manganosite)	Iron manganese oxide phases	Other phases
SCFC	Calcined	✓	–	✓	–	$Mn_xFe_{3-x}O_4$, $(FeO)_x(MnO)_{1-x}$	Ca_2MnO_4, $CaSi_2O_5$
	4.3 (not defluidized)	–	–	–	✓	Mn_2FeO_4	$Fe_{3-x}O_4$, $Fe_{1-x}Mn_x^M$, $CaSiO_3$
EBFC	Calcined	–	✓	✓	–	$Mn_xFe_{3-x}O_4^N$	MgO, K_2O
	4.4 (not defluidized)	–	–	–	✓	$Mn_xFe_{1-x}O^P$	MgO, KO_2

✓: the phase was identified, –: the phase was not identified.

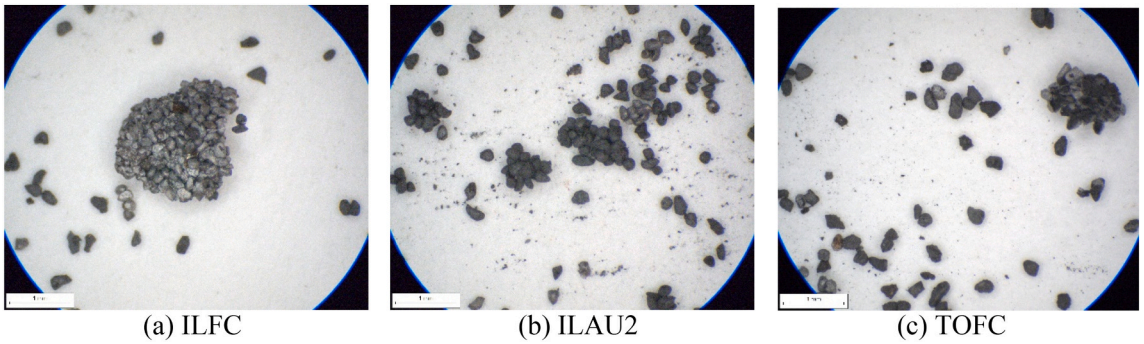

Fig. 8. The light microscope image of the defluidizing oxygen carrier particles.

particles. This observation supports the results discussed in the previous section that the formation of iron on the surface of wüstite is the main factor for promoting particle agglomeration and, eventually, defluidization.

3.5. Elemental distribution in oxygen carriers

Both fresh and defluidized oxygen carriers, with the latter were being in reduced forms, were embedded in epoxy and then analyzed by SEM/EDX to see the elemental distribution across the cross section of the particles using the elemental mapping feature.

Figs. 9 and 10 show that all the elements are distributed throughout the whole particles with strong presence of oxygen in the fresh particles of ILFC and TOFC. This is because the oxygen carriers were in an oxidized state after calcination. However, iron tends to concentrate on the surface of the particles rather than within the bulk particle when they were reduced the furthest and eventually defluidized. This is even more obvious for the ilmenite samples, ILFC and ILAU2, where iron is densely located on the surface joints between two particles and titanium was only detected inside the particles rather than on its surface. Oxygen is distributed quite evenly throughout the oxygen particles. These findings confirm that structural changes have happened under highly reducing conditions, with the stronger indication of iron presence on the particle surface, especially on the interparticle joints. A study by Condori et al. [45] also suggested that iron can migrate from inside to the outer part of the particle under a highly reducing environment.

3.6. Reactivity of oxygen carriers with methane

The reactivity of oxygen carriers was also compared and evaluated based on the methane conversion. Methane could be an important component in biomass volatiles or natural gas [46]. Furthermore, gas phase surroundings are parameters that may have an implication for surface activity [47], which could be related to the phenomena of agglomeration and defluidization. The CO_2-based gas yield and fraction of CO was calculated according to Eq. (6) and (7), respectively, as products of integration. These are plotted as the functions of mass-based conversion. It is important to note that each marker in the graph represent the mean of the calculated values for a methane pulse shown in Table 4. To provide a basis for comparison, the syngas conversions are also plotted in the same way. All of these are shown in Fig. 11.

It can be seen that the CO and CO_2 yield for the methane pulses were quite low, i.e. less than 0.15 for all experiments. The syngas conversions generally declined for all materials as they were gradually reduced. While it can be expected that the methane conversion would usually also decline as the materials were reduced further, some oxygen carriers showed a different trend. One particular material that did so was ilmenite, which comprises ILFC, ILAU1, and ILAU2. It can be seen that the methane conversion for all ilmenite samples to both CO_2 and CO increased at higher reduction degree, particularly after the materials were reduced for about 3%. This trend continued until right before the materials defluidized. The formation of elemental iron at a very high reduction degree could be the reason behind this behavior as iron catalysts have been found to show a high catalytic activity at temperatures above 600 °C [48]. Nevertheless, these higher methane conversions at high reduction degree were still significantly lower than the corresponding syngas conversions at similar degrees of reduction. This was obvious since the strong C—H bonds in methane make it becomes less reactive than syngas [49].

Despite showing defluidization, TOFC showed a stable reactivity toward methane in the generation of CO independently of how much it had been reduced. It could be that the amount of metallic iron formed at this stage was not enough to be able to catalyze methane conversion to a significant extent. The other materials generally showed a decreasing trend for methane conversion to CO_2 but an increasing trend for CO generation. This is obviously due to the oxygen depletion in the particles that had already occurred when they were reduced by syngas, thus the generation of CO was more favorable. Both LDFC and LDAU showed quite a sharp increasing trend in the conversion of methane to CO despite being reduced for only about 1%. The CO generated by the most reduced materials was 2.5–4 times higher than that of the fresh ones. This indicates that LD slag can be a good candidate for oxygen carrier for CLG as the main aim is to produce CO and also H_2. Moreover, the CaO content in LD slag has been shown to have some catalytic properties for the water-gas shift reaction that enhances the CO conversion to H_2 at a temperature of 950 °C [50].

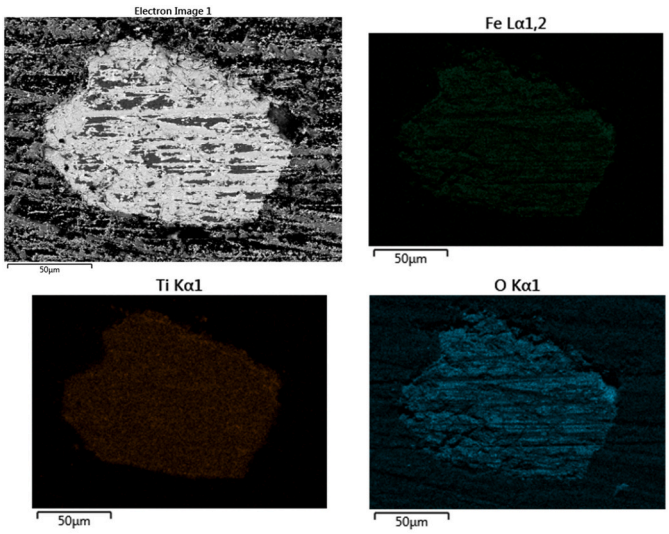

(a) Fresh ILFC

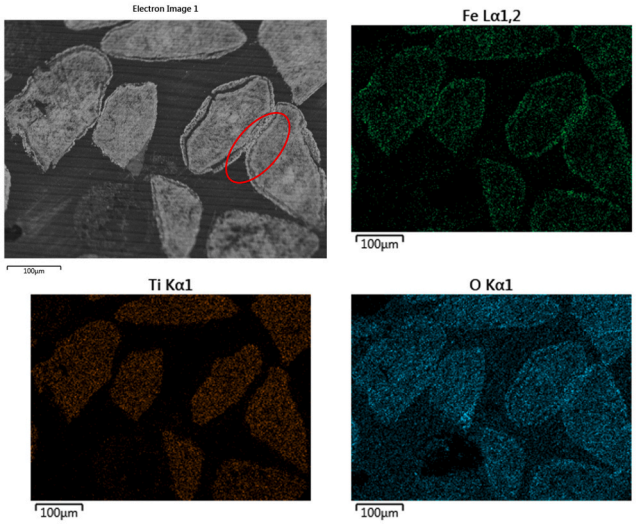

(b) Defluidized ILFC

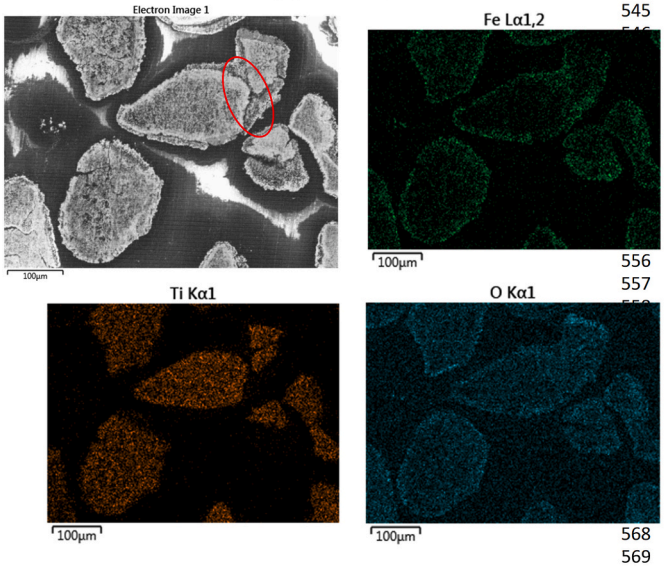

(c) Defluidized ILAU2

Fig. 9. The elemental distribution of iron (Fe), titanium (Ti), and oxygen (O) in fresh and defluidized ilmenite samples. The red circles indicate the surface joints between particles.

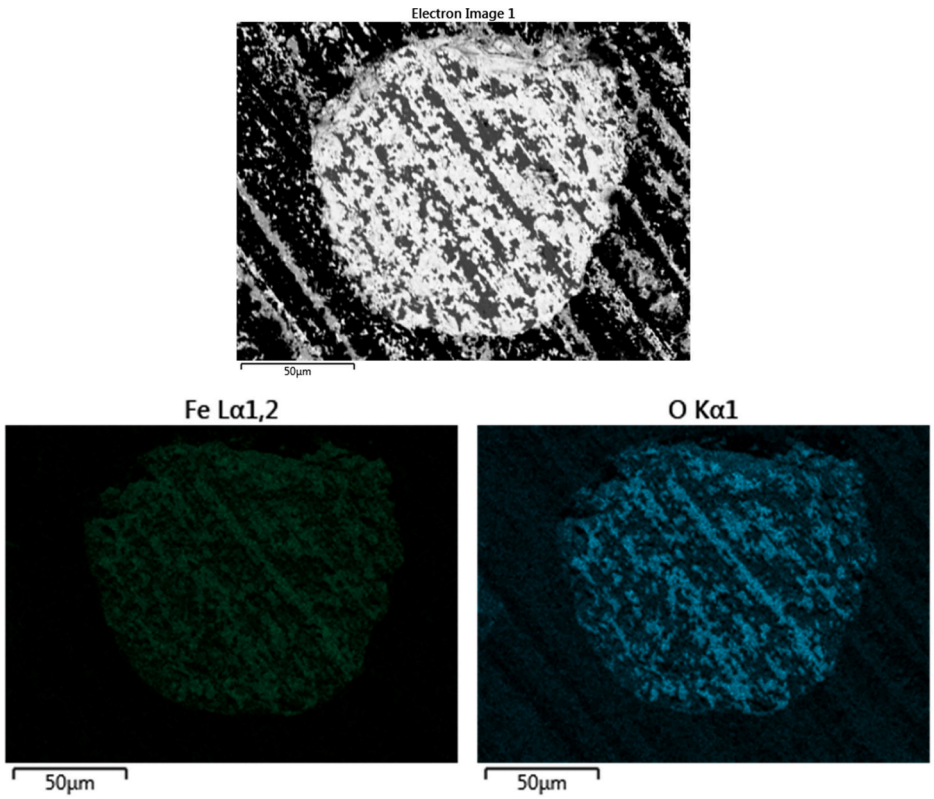

(a) Fresh TOFC

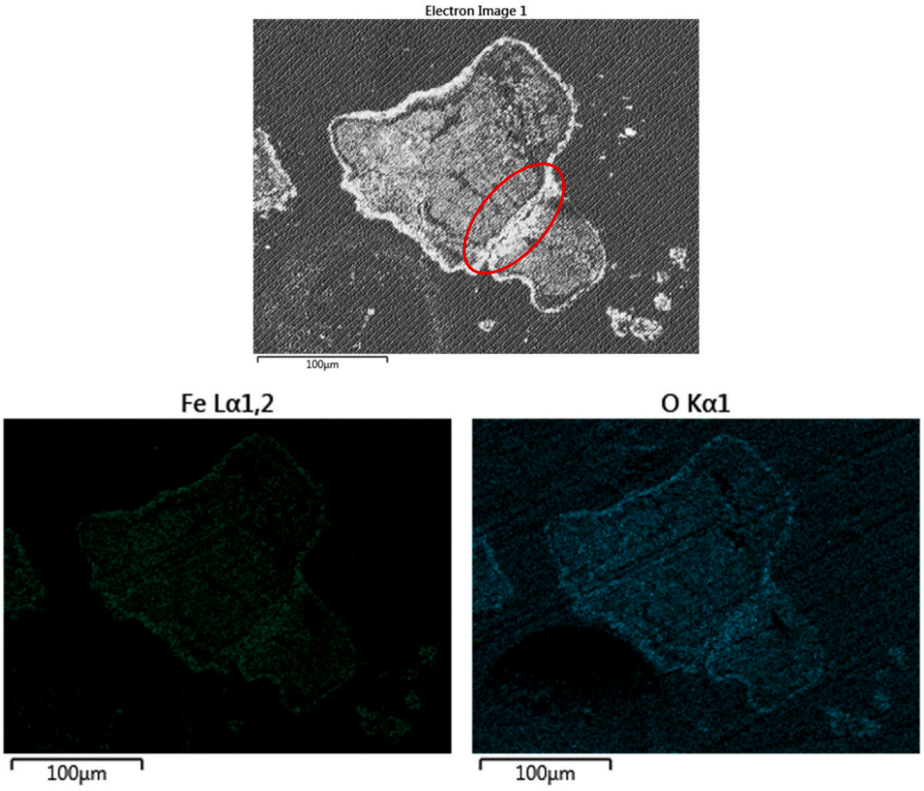

(b) Defluidized TOFC

Fig. 10. The elemental distribution of iron (Fe) and oxygen (O) in TOFC particles. The red circle indicates the surface joint between particles.

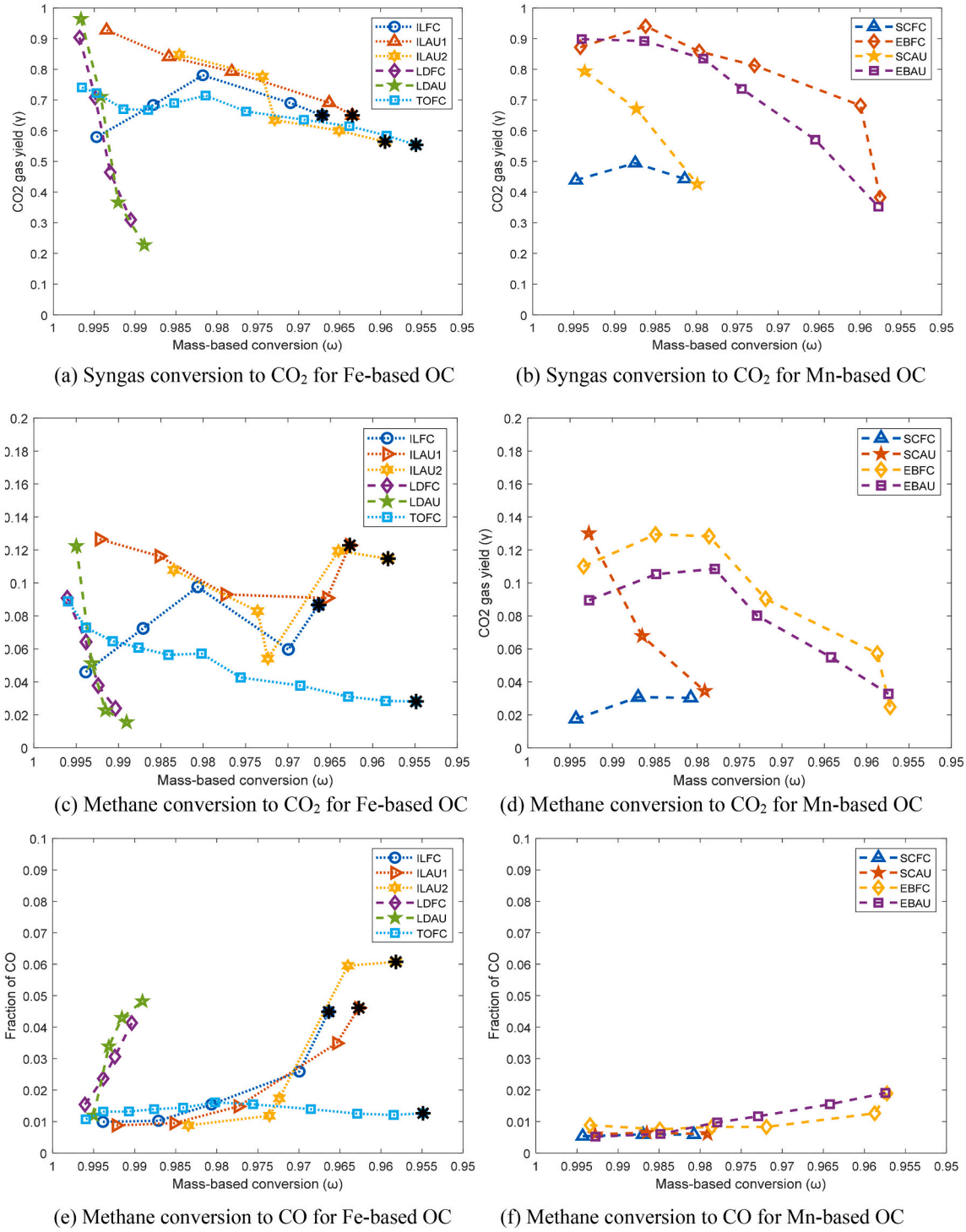

(a) Syngas conversion to CO_2 for Fe-based OC

(b) Syngas conversion to CO_2 for Mn-based OC

(c) Methane conversion to CO_2 for Fe-based OC

(d) Methane conversion to CO_2 for Mn-based OC

(e) Methane conversion to CO for Fe-based OC

(f) Methane conversion to CO for Mn-based OC

Fig. 11. Syngas and methane conversion for iron- and manganese-based OC as a function of mass-based conversion. Symbol * indicated the cycles that were followed by defluidization.

4. Conclusion

This work explores the feasibility to use different natural or waste materials for CLG. More specifically, the investigation is focused on the fluidization behavior and characterization of solid materials at high level of reduction. Under highly reducing conditions, the defluidization occurrence on the iron-based oxygen carriers were more prevalent than on the manganese-based ones. This, however, did not happen to LD slag, which was probably due to its low content of iron. The possible cause of defluidization was the agglomeration of oxygen carrier particles that was triggered by the formation of elemental iron and wüstite as a result of the formed sinter necks that nucleated and grew on the particle surface at high reduction degrees. Lowering the oxidation temperature can in some way reduce the tendency for defluidization. The formation of elemental iron was estimated to take place during the injection of the methane pulse. The presence of manganese phases in the manganese-based oxygen carriers seemed to incorporate the iron to higher oxidation states, preventing the formation of metallic iron and defluidization.

The formation of elemental iron under highly reducing conditions at a high temperature of 900 °C may have catalyzed the methane conversion of iron-based oxygen carriers, thus resulted in a sudden increase of methane conversion at high reduction degrees. As a CLG reactor normally has a rather high steam content, it is questionable if metallic iron can form at normal conditions, yet a local issue in the bed or a situation when the unit is not operated at standard conditions still can create a highly reducing environmentl around the particles.

Notation

CLC	chemical-looping combustion
CLG	chemical-looping gasification
CLR	chemical-looping reforming
n_i	the total outlet molar flow of component i
$\dot{n}$	molar flow of the gas (mol/s)
M_O	molar mass of oxygen (g/mol)
m_{ox}	mass of the oxygen carrier when fully oxidized (g)
OC	oxygen carrier
p_{CO}/p_{CO2}	the ratio of the partial pressure of carbon monoxide to carbon dioxide
T_m	melting point (°C)
t	time (s)
t_{syn}	length of reduction with syngas
U/U_{mf}	ratio of fluidization velocity to minimum fluidization velocity
x_i	fraction of component i
γ_i	gas yield of component i
ω	mass conversion of oxygen carrier
ν	superficial velocity (cm/s)

Declaration of Competing Interest

The authors declare that they have no known competing financial interests or personal relationships that could have appeared to influence the work reported in this paper.

Acknowledgments

This work is a part of the project EU CLARA (Chemical Looping Gasification for Sustainable Production of Biofuels) which has received funding from the European Union's Horizon 2020 research and innovation program under grant agreement No 817841.

Appendix A. Supplementary data

Supplementary data to this article can be found online at https://doi.org/10.1016/j.fuproc.2021.106874.

References

[1] L.H.U.W. Abeydeera, J.W. Mesthrige, T.I. Samarasinghalage, Global research on carbon emissions: a scientometric review, Sustain. 11 (14) (2019) 1–25.
[2] T. Mattison, F. Hildor, Y. Li, C. Linderholm, Negative emissions of carbon dioxide through chemical-looping combustion (CLC) and gasification (CLG) using oxygen carriers based on manganese and iron, Mitig. Adapt. Strateg. Glob. Chang. (Clc) (2019).
[3] A. Abad, Chemical looping for hydrogen production, in: Calcium and Chemical Looping Technology for Power Generation and Carbon Dioxide (CO2) Capture, Elsevier, Cambridge, 2015, pp. 327–374.
[4] T. Mattison, F. Hildor, Y. Li, C. Linderholm, Negative emissions of carbon dioxide through chemical-looping combustion (CLC) and gasification (CLG) using oxygen carriers based on manganese and iron, Mitig. Adapt. Strateg. Glob. Chang. 25 (4) (2020) 497–517.
[5] I. Adánez-Rubio, J.A.C. Ruiz, F. García-Labiano, L.F. de Diego, J. Adánez, Use of bio-glycerol for the production of synthesis gas by chemical looping reforming, Fuel (October) (2020) 119578.
[6] M. Aghabararnejad, G.S. Patience, J. Chaouki, TGA and kinetic modelling of Co, Mn and Cu oxides for Chemical Looping Gasification (CLG), Can. J. Chem. Eng. 92 (11) (2014) 1903–1910.
[7] C. Dong, et al., Deep reduction behavior of iron oxide and its effect on direct CO oxidation, Appl. Surf. Sci. 258 (7) (2012) 2562–2569.
[8] E.R. Stobbe, B.A. De Boer, J.W. Geus, Journal of molecular catalysis A: chemical promotive effect of Bi component on propane partial oxidation over, Int. J. Hydrog. Energy 148–149 (3) (2013) 1557–1566.
[9] M. Zevenhoven, et al., Defluidization of the oxygen carrier ilmenite – Laboratory experiments with potassium salts, Energy 148 (2018) 930–940.
[10] E. Jerndal, T. Mattisson, A. Lyngfelt, C. Combustion, O. After, Chemical Engineering Research and Design 2006-Thermal Analysis of Chemical-Looping Combustion, no. September, 2006.
[11] J. Werther, J. Reppenhagen, Attrition in Fluidized Beds and Pneumatic Conveying Lines, Noyes Publications, 1999.
[12] M. Rydén, P. Moldenhauer, S. Lindqvist, T. Mattisson, A. Lyngfelt, Measuring attrition resistance of oxygen carrier particles for chemical looping combustion with a customized jet cup, Powder Technol. 256 (2014) 75–86.
[13] T.A. Brown, F. Scala, S.A. Scott, J.S. Dennis, P. Salatino, The attrition behaviour of oxygen-carriers under inert and reacting conditions, Chem. Eng. Sci. 71 (2012) 449–467.
[14] P. Cho, T. Mattisson, A. Lyngfelt, Defluidization conditions for a fluidized bed of iron oxide-, nickel oxide-, and manganese oxide-containing oxygen carriers for chemical-looping combustion, Ind. Eng. Chem. Res. 45 (3) (2006) 968–977.
[15] H. Leion, V. Frick, F. Hildor, Experimental method and setup for laboratory fluidized bed reactor testing, Energies 11 (10) (2018).
[16] D. Mei, A.H. Soleimanisalim, C. Linderholm, A. Lyngfelt, T. Mattisson, Reactivity and lifetime assessment of an oxygen releasable manganese ore with biomass fuels in a 10 kWth pilot rig for chemical looping combustion, Fuel Process. Technol. 215 (February) (2021) 106743.
[17] H. Leion, T. Mattisson, A. Lyngfelt, Use of ores and industrial products as oxygen carriers in chemical-looping combustion, Energy Fuel 23 (4) (2009) 2307–2315.
[18] C. Linderholm, M. Schmitz, Chemical-looping combustion of solid fuels in a 100 kW dual circulating fluidized bed system using iron ore as oxygen carrier, J. Environ. Chem. Eng. 4 (1) (2016) 1029–1039.
[19] F. Störner, F. Hildor, H. Leion, M. Zevenhoven, L. Hupa, M. Rydén, Potassium ash interactions with oxygen carriers steel converter slag and iron mill scale in chemical-looping combustion of biomass-experimental evaluation using model compounds, Energy Fuel 34 (2) (2020) 2304–2314.
[20] S. Sundqvist, T. Mattisson, H. Leion, A. Lyngfelt, Oxygen release from manganese ores relevant for chemical looping with oxygen uncoupling conditions, Fuel 232 (June) (2018) 693–703.
[21] Y. Yan, T. Mattisson, P. Moldenhauer, E.J. Anthony, P.T. Clough, Applying machine learning algorithms in estimating the performance of heterogeneous, multi-component materials as oxygen carriers for chemical-looping processes, Chem. Eng. J. 387 (January) (2020) 124072.
[22] J. Adánez, A. Cuadrat, A. Abad, P. Gayán, L.F.D. Diego, F. García-Labiano, Ilmenite activation during consecutive redox cycles in chemical-looping combustion, Energy Fuel 24 (2) (2010) 1402–1413.
[23] A. Hedayati, A. H. Soleimanisalim, C. J. Linderholm, T. Mattisson, and A. Lyngfelt, "Thermochemical Conversion of Biomass Volatiles via Chemical Looping with Steel Converter Waste Materials as Oxygen Carrier, (Submitted for publication)".
[24] A. Hedayati, A.H. Soleimanisalim, C.J. Linderholm, T. Mattisson, A. Lyngfelt, Experimental evaluation of manganese ores for chemical looping conversion of synthetic biomass volatiles in a 300 W reactor system, J. Environ. Chem. Eng. 9 (2) (2021) 105112.
[25] C. Linderholm, E. Jerndal, T. Mattisson, A. Lyngfelt, Investigation of NiO-based mixed oxides in a 300-W chemical-looping combustor, Chem. Eng. Res. Des. 88 (5–6) (2010) 661–672.
[26] D. Gidaspow, The fluidized state, in: Multiphase Flow and Fluidization, 1st ed., Academic Press, Inc., Chicago, 1994, pp. 97–114.
[27] D. Yamaguchi, L. Tang, K. Chiang, Pre-oxidation of natural ilmenite for use as an oxygen carrier in the cyclic methane–steam redox process for hydrogen production, Chem. Eng. J. 322 (2017) 632–645.
[28] F. García-Labiano, L.F. De Diego, J. Adánez, A. Abad, P. Gayán, Temperature Variations in the Oxygen Carrier Particles During Their Reduction and Oxidation in a Chemical-Looping Combustion System 60, 2005 no. 3.
[29] Y. Zhong, Z. Wang, Z. Guo, Q. Tang, Defluidization behavior of iron powders at elevated temperature: Influence of fluidizing gas and particle adhesion, Powder Technol. 230 (2012) 225–231.
[30] A. Mehdilo, M. Irannajad, Effects of mineralogical and textural characteristics of ilmenite concentrate on synthetic rutile production, Arab. J. Geosci. 6 (10) (2013) 3865–3876.
[31] S.K. Gupta, V. Rajakumar, P. Grieveson, Phase transformations during heating of llmenite concentrates, Metall. Trans. B 22 (5) (1991) 711–716.
[32] A. Pineau, N. Kanari, I. Gaballah, Kinetics of reduction of iron oxides by H2. Part II. Low temperature reduction of magnetite, Thermochim. Acta 456 (2) (2007) 75–88.
[33] D.R. Gaskell, D.E. Laughlin, Introduction to the Thermodynamics of Materials, 6th ed., CRC Press, Taylor & Francis, Boca Raton, 2018.
[34] R.H. Perry, D.W. Green, J.O. Maloney, Perry's Chemical Engineers' Handbook, 8th ed., McGraw Hill, New York, 2008.
[35] D.R. Lide, G. Baysinger, Physical constants of organic compounds, CRC Handb. Chem. Phys. (2019), 3–1–3–576.
[36] P.S. Liu, G.F. Chen, Making porous metals, in: Porous Materials, 1st ed., Elsevier Inc., Waltham, 2014, pp. 21–112.
[37] C.M. Kramer, R.M. German, Low-Temperature Sintering of Iron Oxides 1, 1978, pp. 340–342.
[38] J.A. Moulijn, A.E. Van Diepen, F. Kapteijn, Catalyst deactivation: is it predictable? What to do? Appl. Catal. A Gen. 212 (1–2) (2001) 3–16.

[39] W. Liu, J.Y. Lim, M.A. Saucedo, A.N. Hayhurst, S.A. Scott, J.S. Dennis, Kinetics of the reduction of wüstite by hydrogen and carbon monoxide for the chemical looping production of hydrogen, Chem. Eng. Sci. 120 (2014) 149–166.
[40] L. Guo, S. Zhong, Q. Bao, J. Gao, Z. Guo, Nucleation and growth of iron whiskers during gaseous reduction of hematite iron ore fines, Metals (Basel) 9 (7) (2019).
[41] M. Hamidi, V.M. Wheeler, X. Gao, J. Pye, K. Catchpole, A.W. Weimer, Reduction of iron–manganese oxide particles in a lab-scale packed-bed reactor for thermochemical energy storage, Chem. Eng. Sci. 221 (2020) 115700.
[42] Y. Zhang, M. Du, B. Liu, Z. Su, G. Li, T. Jiang, Separation and recovery of iron and manganese from high-iron manganese oxide ores by reduction roasting and magnetic separation technique, Sep. Sci. Technol. 52 (7) (2017) 1321–1332.
[43] J.W. Anthony, R.A. Bideaux, K.W. Bladh, M.C. Nichols, Iron, in: Handbook of Mineralogy, Mineral Data Publishing, Tucson, 2001.
[44] J.W. Anthony, R.A. Bideaux, K.W. Bladh, M.C. Nichols, Wustite, in: Handbook of Mineralogy, Mineral Data Publishing, Tucson, 2001.
[45] O. Condori, F. García-Labiano, L.F. de Diego, M.T. Izquierdo, A. Abad, J. Adánez, Biomass chemical looping gasification for syngas production using ilmenite as oxygen carrier in a 1.5 kWth unit, Chem. Eng. J. 405 (July 2020) (2021) 126679.
[46] A. Skorek, R. Włodarczyk, The use of methane in practical solutions of environmental engineering, J. Ecol. Eng. 19 (2) (2018) 172–178.
[47] X. Zhu, Q. Imtiaz, F. Donat, C.R. Müller, F. Li, Chemical looping beyond combustion-a perspective, Energy Environ. Sci. 13 (3) (2020) 772–804.
[48] N.Z. Muradov, How to produce hydrogen form fossil fuels without CO2 emission, Int. J. Hydrog. Energy 18 (3) (1993) 211–215.
[49] C. Li, CH Bond Activation of Methane and Unsaturated Molecules by a Transient eta2-Cyclopropene Complex of Niobium : Synthesis, Characterization and Mechanistic Studies, The University of Toulouse, 2015.
[50] F. Hildor, T. Mattisson, H. Leion, C. Linderholm, M. Rydén, Steel converter slag as an oxygen carrier in a 12 MWth CFB boiler – Ash interaction and material evolution, Int. J. Greenh. Gas Control 88 (July) (2019) 321–331.